

# Atomic Comagnetometer with a Closed-Loop Optically Aligned $^{87}\text{Rb}$ Dual-Frequency Oscillator

Zhiguo Wang<sup>1,2</sup>, Xiang Peng<sup>1,3</sup>, Zhiqiang Xiong,<sup>1</sup> Jintao Zheng,<sup>1</sup> Hui Luo,<sup>1,2,\*</sup> and Hong Guo<sup>1,3,†</sup>

<sup>1</sup>*College of Advanced Interdisciplinary Studies, National University of Defense Technology, Changsha 410073, People's Republic of China*

<sup>2</sup>*Interdisciplinary Center of Quantum Information, National University of Defense Technology, Changsha 410073, People's Republic of China*

<sup>3</sup>*State Key Laboratory of Advanced Optical Communication Systems and Networks, Department of Electronics, and Center for Quantum Information Technology, Peking University, Beijing 100871, People's Republic of China*

(Received 8 August 2022; revised 22 November 2022; accepted 12 January 2023; published 8 February 2023)

Comagnetometers have been widely used in fundamental research, such as tests of spin-gravity coupling and searches for permanent electric dipole moments (EDMs). Here, we report a comagnetometer that consists of simultaneous closed-loop oscillation of the  $F = 1$  and  $F = 2$  hyperfine Zeeman transitions of optically aligned  $^{87}\text{Rb}$  atoms. The Allan deviation of the  $F = 2$  and  $F = 1$  oscillation-frequency ratio reaches  $1 \times 10^{-9}$  after running continuously for 2 days, corresponding to a sensitivity of approximately  $4 \times 10^{-19}$  eV for the measurement of the hypothetical spin-dependent gravitational energy of the proton. The long-term stability of the comagnetometer can be further improved by system-level thermal control and optimization of the experimental parameters.

DOI: 10.1103/PhysRevApplied.19.024021

## I. INTRODUCTION

Atomic spin precesses in a magnetic field with a frequency that is almost proportional to the magnitude of the magnetic field, so it can be used as an atomic magnetometer [1,2]. The precession frequency, however, also contains the contribution from possible rotation rates with respect to the inertial space as well as the hypothesized exotic physical effects [3–6]. In the vast majority of cases, the contribution from the magnetic field to the precession frequency is much larger than that from the other physical effects, even if the spins are placed in a high-performance magnetic shield. Therefore, when measuring physical quantities except for the magnetic field, researchers usually use the comagnetometer, which consists of two magnetometers occupying the same space to common-mode reject the magnetic field fluctuations [5–9]. At present, various comagnetometers have been proposed. With respect to the spin species, there are groups of  $^3\text{He}$ - $^{129}\text{Xe}$  [5,6],  $^{129}\text{Xe}$ - $^{131}\text{Xe}$  [8], K- $^3\text{He}$  [9], etc. With respect to the operation mode, there are the continuous mode, which is also called the maser or oscillator [6,10–13], the pulse mode and/or the free-precession decay mode [5,8,14–17], and the magnetic resonance scanning (MSR) mode [18]. We

have previously proposed a single-species comagnetometer with the MSR mode based on the hyperfine levels of  $^{87}\text{Rb}$  atoms in a paraffin-coated cell [18]. It shows almost negligible sensitivity to variations of the laser power and frequency, the magnetic field, and the magnetic field gradients. However, the MSR method leads to a reduction in sensitivity, since it takes a scanning cycle to obtain only one magnetic resonance frequency. Moreover, it acquires the magnetic resonance frequencies of the two hyperfine levels asynchronously, which cannot efficiently suppress magnetic noise.

In this paper, we improve the single-species comagnetometer with the MSR mode into an optically aligned dual-oscillator comagnetometer (OADOC), so that issues such as inefficiency and nonsimultaneity in data acquisition are addressed. Meanwhile, we keep using the optically aligned magnetometer configuration instead of an optically oriented magnetometer to avoid the light shift due to circularly polarized pump light [18]. The aligned magnetometer can be dated back to the pioneering work by Bell and Bloom [19] and has recently been studied in depth by Weis *et al.* [20–24]. Our comagnetometer is slightly different from theirs in that the laser frequency should be tuned several gigahertz off resonant to obtain two Zeeman transitions of  $^{87}\text{Rb}$  atoms simultaneously, as we have done in Ref. [18]. The OADOC preserves the advantages of immunity to variations of the laser parameters. In our experiment, the spin precession-frequency ratio of  $F = 2$

\*Corresponding author. Email: luohui.luo@163.com

†Corresponding author. Email: hongguo@pku.edu.cn

and  $F = 1$  ground-state hyperfine levels reaches  $2 \times 10^{-9}$  with a free-running leading magnetic field and  $1 \times 10^{-9}$  with a stabilized leading magnetic field, respectively, 5–10 times better in stability than our previous result [18]. The OADOC not only shows the possibility of improving the laboratory constraints on spin-gravity interactions of the proton by several times [25] but also has potential applications in the measurement of axion-nucleon and axion-electron interactions [13,26].

## II. METHODS

The experimental setup of the comagnetometer is similar to our previous one [18] except that here we use an HF2LI (Zurich Instruments) rather than a lock-in amplifier (LIA) programmed using the LabVIEW™ software to manipulate the spins, as shown in Fig. 1. Besides the ordinary LIA module, the HF2LI also contains two phase-locked loop (PLL) modules and four proportional-integral-differential (PID) modules. We can program the HF2LI using its accessory software, called LabOne. The “Sel” switch is the functional switch between an LIA and two PLLs. The signal-in (“Sig In”) port of the HF2LI is connected to the polarimetric signal and the signal-output (“Sig Out”) port is connected to the  $X$  coil. A block diagram of the LIA module is shown in Fig. 1(b): the outputs, i.e.,  $X$ ,  $Y$ ,  $R$ , and  $\theta$ , can be recorded simultaneously. Block diagrams of two PLLs are shown in Fig. 1(c). PLL<sub>1</sub> and PLL<sub>2</sub> are used to track the magnetic resonance frequencies of  $F = 1$  and  $F = 2$ , respectively. For each PLL, we can set parameters such as the center frequency, the locking range, the bandwidth, and the phase shift. We take PLL<sub>1</sub> as an example to briefly introduce the operating principle of the spin oscillator. With a mixer, a low-pass filter (LPF), and a phase detector (PD), we can obtain the relative phase between the magnetic resonance signal and the numerically controlled oscillator (NCO). The phase difference between the set phase  $\phi_{\text{ref}1}$  and the PD output gives a phase error  $e_{\phi 1}$ , which is sent to a PID module to produce a driving signal for the NCO. After choosing suitable parameters, the oscillating frequency of PLL<sub>1</sub> is locked to the magnetic resonance frequency of  $F = 1$ . The sine-wave outputs of two NCOs can be added in the HF2LI before they are sent out through the Sig Out port as a driving field. More details can be found in the HF2LI User Manual [27].

By toggling the Sel switch in the HF2LI to the LIA module, applying an oscillating magnetic field  $B_x = B_1 \cos(2\pi f_d t)$  in the  $X$  coil, and a scanning frequency  $f_d$  and recording the outputs of the  $X$ ,  $Y$ , and  $R$  channels simultaneously, we can obtain the magnetic resonance signals. By toggling the Sel switch to the PLLs and selecting the proper parameters, we can make the PLLs track the magnetic resonance frequencies of  $^{87}\text{Rb}$  atoms continuously. The frequencies  $f_1$  and  $f_2$  of the two PLLs

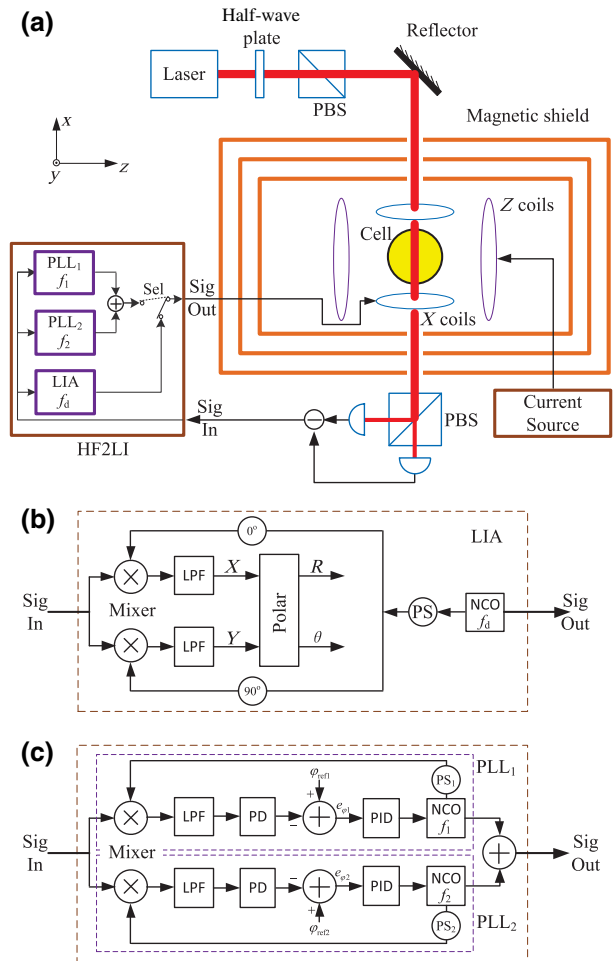


FIG. 1. (a) The experimental setup of the comagnetometer. The polarization of a distributed feedback laser is purified by a polarizing beam splitter (PBS). The laser power can be adjusted with a half-wave plate. After traversing the cell, the laser is split by a PBS and impinges on two photodiodes that form a polarimeter. The polarimetric signal is sent to the signal-in (Sig In) port of the HF2LI, the signal-out (Sig Out) port of which is connected to the  $X$  coil. The leading magnetic field is produced by the  $Z$  coil, driven by a current source. The HF2LI contains an ordinary lock-in amplifier (LIA) module and two modules of PLLs (PLL<sub>1</sub> and PLL<sub>2</sub>). The functioning of the HF2LI can be programmed such that operations of both frequency scanning by LIA and closed-loop oscillation by PLL<sub>1</sub> and PLL<sub>2</sub> can be toggled with a switch (Sel).  $f_d$  is the scanning frequency of the LIA.  $f_1$  and  $f_2$  are the output frequencies of PLL<sub>1</sub> and PLL<sub>2</sub>, respectively. (b) A block diagram of the LIA module: NCO, numerically controlled oscillator; PS, phase shift; LPF, low-pass filter. (c) A block diagram of the PLLs module: PD, phase detector.

are recorded simultaneously as the output of the dual-frequency oscillator. All the experiments are completed at ambient temperature ( $24 \pm 1$ ) °C, which is controlled by an air conditioner.

At first, we obtain the magnetic resonance signals for  $F = 1$  and  $F = 2$  Zeeman transitions of  $^{87}\text{Rb}$  atoms with

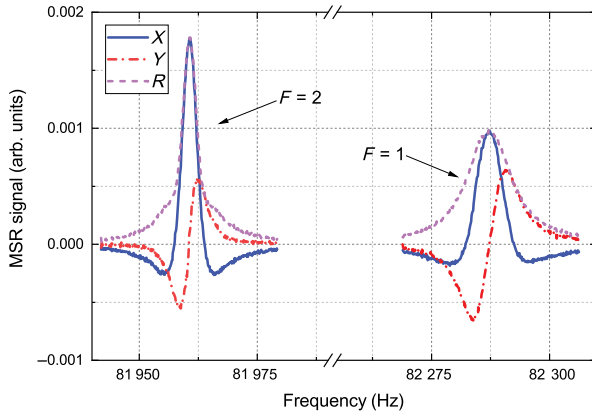


FIG. 2. The magnetic resonance signals for the  $F = 1$  and  $F = 2$  Zeeman transitions. The markers  $X$ ,  $Y$ , and  $R$  denote the corresponding channels of the LIA module when the driving frequency  $f_d$  is scanned. For these data, the laser power is adjusted to 1 mW and the laser frequency is tuned to 1.3 GHz above the  $F = 1 \rightarrow F'$  transitions of the  $^{87}\text{Rb}$   $D_2$  line at a driving voltage of  $B_1 = 0.1$  nT, where  $F'$  denotes the hyperfine levels of the  $5P_{3/2}$  level.

the LIA module, as shown in Fig. 2. The zero-crossing points of the  $Y$  signals correspond to resonant frequencies. The two Zeeman transitions have a frequency splitting of approximately 326.4 Hz, with a leading field of  $11.71\ \mu\text{T}$ , much larger than the magnetic resonance line widths. Therefore, we can operate the two Zeeman transitions as two almost independent oscillators.

The sensitivity of the aligned magnetometer depends on many parameters, such as the laser power and frequency and the amplitude of the driving field [23,24]. We use the noise-equivalent magnetic field (NEM) given in Ref. [23] as the measure for roughly optimizing the sensitivity. This can be expressed as

$$\text{NEM} = \frac{\rho_S}{|t_w|}, \quad (1)$$

where  $\rho_S$  is the root spectral density of the photocurrent shot noise and  $t_w$  is the derivative of the dispersive experimental magnetic resonance line shape with respect to the leading magnetic field on resonance. According to Eqs. (9) and (14) in Ref. [23],  $\rho_S$  can be expressed as

$$\rho_S = C_1 \sqrt{P_L}, \quad (2)$$

and  $t_w$  can be expressed as

$$t_w = \frac{g(P_L)h\Gamma_0(\Gamma_2^2 - 2\omega_1^2)\omega_1}{(\Gamma_1\Gamma_2 + \omega_1^2)[\Gamma_0\Gamma_1\Gamma_2 + (\Gamma_0 + 3\Gamma_2)\omega_1^2]}. \quad (3)$$

In Eq. (2),  $C_1$  is a constant for a given photodiode and  $P_L$  is the laser power. In Eq. (3),  $g(P_L)$  is a factor relating

to  $P_L$ ,  $h = 9/16$  in our case,  $\omega_1 = \gamma B_1$  is the Rabi frequency of the radio-frequency field,  $\gamma$  is the gyromagnetic ratio, and  $\Gamma_0$ ,  $\Gamma_1$ , and  $\Gamma_2$  are three line-width parameters. In Ref. [23], the  $g(P_L)$  factor is given by

$$g(P_L) = C_2 \frac{P_L^2}{(P_{S1} + P_L)(P_{S2} + P_L)}, \quad (4)$$

where  $C_2$  is a constant and  $P_{S1}$  and  $P_{S2}$  are saturation powers that can be determined by experiment. As an estimate, we might as well let  $\Gamma_0 = \Gamma_1 = \Gamma_2 = \Gamma$ . The magnetic resonance line width, which depends on the laser power  $P_L$ , can be expressed as

$$\Gamma(P_L) = \Gamma_{00} + \alpha P_L + \beta P_L^2, \quad (5)$$

where  $\Gamma_{00}$  is the intrinsic line width without optical-power broadening ( $P_L = 0$ ) and  $\alpha$  and  $\beta$  are two parameters that can be determined by experiment [23].

Combining Eqs. (1)–(5), we can obtain an empirical expression for the NEM:

$$\frac{1}{\text{NEM}} = C \frac{P_L^{3/2}}{(P_{S1} + P_L)(P_{S2} + P_L)} \frac{(\Gamma^2 - 2\omega_1^2)\omega_1}{(\Gamma^2 + \omega_1^2)(\Gamma^2 + 4\omega_1^2)}, \quad (6)$$

where  $C = 9C_2/16C_1$ . This empirical expression shows that there is an optimized NEM at some laser power  $P_L$  and driving magnetic field  $B_1$  in the alignment magnetometers [23].

We optimize the NEM experimentally with the magnetic resonance signals under different conditions, as shown in Fig. 3. At  $B_1 = 0.1$  nT, the laser frequency is calibrated by a vacuum Rb cell, while the laser power is changed by rotating the half-wave plate before the PBS. Here, we define the laser detuning  $\Delta$  as the difference between the laser frequency and the transition frequency of the  $F = 1 \rightarrow F'$  transition of the  $^{87}\text{Rb}$   $D_2$  line. It is shown in Fig. 3(a) that the NEM for the  $F = 2$  magnetic resonance is better than that of the  $F = 1$  with the experimental parameters, mainly because more atoms are populated on the  $F = 2$  level. Thus, the optimization of the NEM for  $F = 1$  is the key factor taken into account. We reject the detuning  $\Delta_2$  at first, since it gives the worst NEM for the  $F = 1$  magnetic resonance. We choose the detuning  $\Delta_3$ , since the NEM of  $F = 1$  at  $\Delta_3$  is slightly better than that at  $\Delta_1$ , with the laser power in the range of 1.0–1.5 mW. We choose the laser power of 1 mW, since the NEM in the range of 1.0–1.5 mW is almost the same but low power gives a small tensor light shift [28]. According to Fig. 3(b), the NEM of  $F = 1$  decreases slightly with  $B_1$ , while that of  $F = 2$  increases relatively remarkably, since the line widths of the two Zeeman transitions are different. According to Eq. (6), the optimized  $B_1$  depends on the line width of the magnetic resonance. In the range of

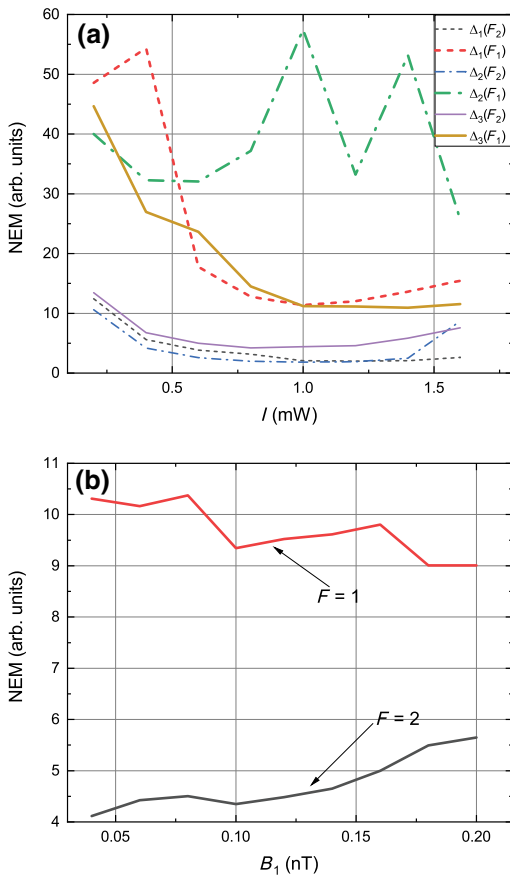


FIG. 3. The experimental optimization of the noise-equivalent magnetic field (NEM). (a) The NEM as a function of the light power and frequency at  $B_1 = 0.1$  nT. In the legend,  $\Delta$  denotes laser detuning and  $\Delta_1$ ,  $\Delta_2$ , and  $\Delta_3$  correspond to 1.2, 2.6, and 1.5 GHz above the  $F = 1 \rightarrow F'$  transitions of the  $^{87}\text{Rb}$   $D_2$  line, respectively. The marks  $F_1$  and  $F_2$  in parentheses denote the two hyperfine ground states, respectively. (b) The NEM as a function of the amplitude of the driving field when the laser power is adjusted to 1 mW and the laser frequency is tuned to 1.5 GHz above the  $F = 1 \rightarrow F'$  transitions of the  $^{87}\text{Rb}$   $D_2$  line.

0.1–0.2 nT, the NEM of  $F = 1$  does not change so much but the small driving field gives a small Bloch-Siegert shift [29]. Thus we choose  $B_1 = 0.1$  nT so as to make a compromise between the signal-to-noise ratio (SNR) and the Bloch-Siegert shift. With these optimized parameters, the magnetic resonance line widths are approximately 2.6 Hz and 7.3 Hz for  $F = 2$  and  $F = 1$ , respectively. Note that in order to obtain dual-frequency oscillation, we tune the laser frequency away from the optical resonance of both  $F = 1$  and  $F = 2$  in ground-state hyperfine levels to the upper levels of the  $D_2$  line. This will make the characteristics of each magnetometer different from those of common alignment magnetometers, especially the NEM [23]. However, qualitatively—taken as a whole—these experimental results are consistent with the empirical expression in Eq. (6).

We construct two oscillators using the PLLs in the HF2LI. The parameters of the two PLLs are identical except for the center frequencies, which are set according to the corresponding magnetic resonance frequencies from Fig. 2 and the reference phases  $\phi_{\text{ref}1}$  and  $\phi_{\text{ref}2}$ , which are set to maximize the amplitudes of the two oscillators, respectively. Each PLL has the following parameters: a locking range of 50 Hz; an eighth-order low-pass filter with a corner frequency of 50 Hz; and  $P$ ,  $I$ , and  $D$  parameters for the NCO of 0.15, 0.1, and 0, respectively.

The frequencies of the dual-frequency oscillator recorded at 14 samples/s are shown in Fig. 4(a). The measured average value of the two frequency ratios,  $F_r = f_2/f_1$ , is 0.9960375. Here,  $f_2$  and  $f_1$  are the oscillation frequencies from the  $F = 2$  and  $F = 1$  oscillators, respectively. Also, a frequency  $f_c = f_2 - f_1/0.9960375$  is defined as the output of the comagnetometer. Note that  $F_r$  deviates from its theoretical value of 0.9960339 by  $3.6 \times 10^{-6}$ . The main reason for this deviation is the frequency shift in the oscillator

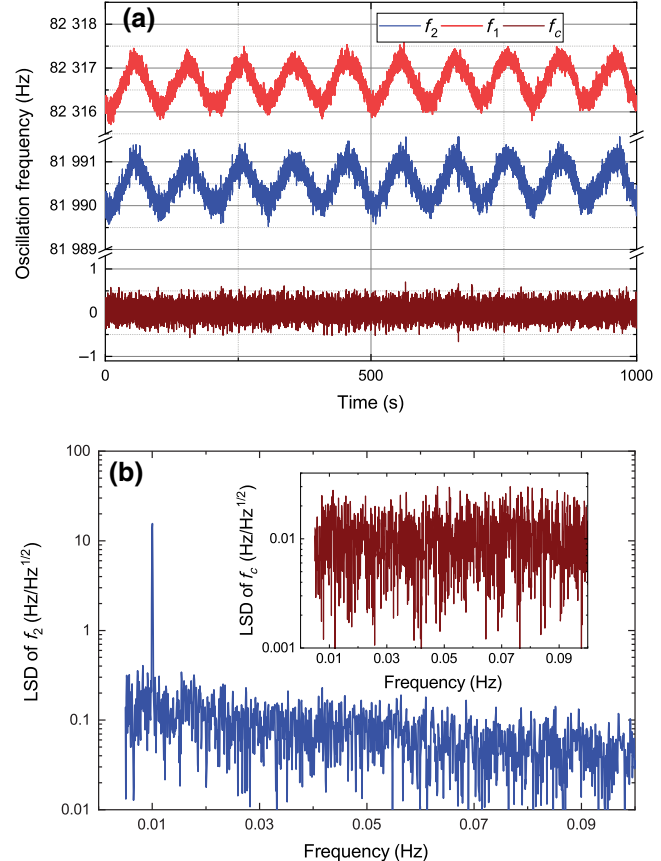


FIG. 4. The frequencies of the dual oscillators recorded by the HF2LI when a 0.01-Hz weak artificial magnetic field is added to the leading magnetic field. (a) The time-domain data at 14 samples/s, where  $f_1$  (blue line) and  $f_2$  (red line) correspond to the oscillation frequency of the magnetic resonance in the  $F = 1$  and  $F = 2$  hyperfine levels, respectively.  $f_c = f_2 - f_1/0.9960375$  (brown line). (b) The linear spectrum density (LSD) of  $f_2$  and  $f_c$ .

operation, by which the relative phase  $\Delta\phi$  between the precession and driving field contributes to a frequency shift of  $\Gamma \tan(\Delta\phi)/(2\pi)$  [3,29]. A deviation of  $3.6 \times 10^{-6}$  for  $F_r$  corresponds to a relative phase error of approximately  $\pm 2^\circ$ , which is within the phase uncertainty caused by our method in setting the PLL phase. According to Eq. (5), the line widths depend on the laser parameters, which also results in  $F_r$  deviation. We carry out a perturbation experiment, which shows that  $F_r$  has a rate of change of  $2.9 \times 10^{-8}/\text{mW}$  for the laser power and of  $1.2 \times 10^{-10}/\text{MHz}$  for the laser frequency with our experimental parameters. The interference between the two hyperfine Zeeman transitions might also lead to frequency shifts that cannot be common-mode rejected.

In order to check the effect on suppressing magnetic field fluctuations, a weak artificial magnetic field of 0.7 nT, varying sinusoidally at 0.01 Hz, is added on the leading magnetic field. The 0.01-Hz frequency modulation can be clearly seen in the time-domain frequencies of  $f_1$  and  $f_2$  but not in  $f_c$ , as shown in Fig. 4(a). The linear spectrum density (LSD, or the square root of the power spectral density) of  $f_2$  and  $f_c$  is shown in Fig. 4(b). We cannot find the 0.01-Hz frequency peak in the LSD of  $f_c$  and thus the suppression of magnetic fluctuations is at least by a factor of 500. When increasing the amplitude of the artificial magnetic field to 7 nT, we obtain a common-mode rejection ratio of roughly 750. However, some kinds of nonlinearity appear, e.g., amplitude modulation of the NCO with harmonics of 0.01 Hz. This reduces the ability of the OADOC to suppress relatively strong magnetic fluctuations. The ability to suppress magnetic field fluctuations is also limited by the frequency-response characteristic of the spin oscillator [3], since the line width and the SNR of the two oscillators are not identical. The LSD of  $f_c$  gives a noise floor of approximately  $0.01 \text{ Hz}/\text{Hz}^{1/2}$ , corresponding to an equivalent magnetic sensitivity of  $1.4 \text{ pT}/\text{Hz}^{1/2}$ , much less than the sensitivity of a common alignment magnetometer [23].

### III. RESULTS AND DISCUSSION

The comagnetometer based on dual oscillators can be used to test the spin-gravity interaction through its frequency ratio [13,30,31]. In order to evaluate the long-term stability, we record the dual frequencies over a time duration of 12 h. The drifts of  $f_2/\langle f_2 \rangle$ ,  $f_1/\langle f_1 \rangle$ , and  $F_r$  are evaluated by means of the Allan deviation, as shown in Fig. 5. Note that only 32 768 s of the 12-h-length data are used, since we separate the data into segments with points of powers of 2 to calculate the Allan deviation. Here,  $\langle x \rangle$  denotes the average of  $x$ . The Allan deviations of  $f_2/\langle f_2 \rangle$  and  $f_1/\langle f_1 \rangle$  are centered on  $10^{-6}$ . They indicate that the relative drift of the leading magnetic field is roughly  $10^{-6}$ . The Allan deviation of  $F_r$  reaches  $2 \times 10^{-9}$  after an integration time of  $4 \times 10^3$  s. Since the noise contribution

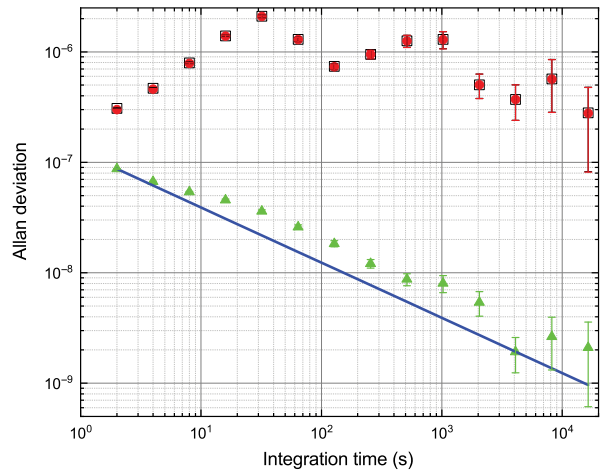


FIG. 5. The Allan deviation of the relative frequencies of the dual oscillators with a free-running leading magnetic field: open black squares,  $f_1/\langle f_1 \rangle$ ; red circles,  $f_2/\langle f_2 \rangle$ ; green triangles,  $F_r$ . The blue line shows the Allan deviation of  $F_r$  estimated by the noise floor of  $f_c$ . The  $1\sigma$  confidence interval of the Allan deviation is estimated according to Ref. [33].

from each magnetometer to  $F_r$  is approximately equal to  $f_c/\langle f_1 \rangle$ , we use the noise floor of  $f_c$  divided by  $\langle f_1 \rangle$  and  $\tau^{1/2}$  to estimate the Allan deviation of  $F_r$  due to white noise (solid line in Fig. 5). Comparing this with the experimental Allan deviation, we find that there is still low-frequency drift in  $F_r$ . This comes partly from the drift of the leading magnetic field and partly from the drift of the laser parameters. Overall, the comagnetometer shows remarkable suppression to low-frequency drift, since the Allan deviation of  $F_r$  decreases even at  $1.6 \times 10^4$  s. According to the Allan deviations of  $f_2/\langle f_2 \rangle$  and  $f_1/\langle f_1 \rangle$ , we find that there are low-frequency noises in the leading magnetic field at different time scales, which breaks the hypothetical power-law precondition of the Allan deviation [32].

We can also operate the comagnetometer with the leading magnetic field stabilized. This can be done by employing a feedback control loop that locks the frequency of either oscillator to a stable reference frequency [34]. Meanwhile, the frequencies of the dual oscillators are recorded. The experiment is implemented with a PID module in the HF2LI, which locks frequency  $f_2$  to a reference frequency of 81 990 Hz. The Allan deviations of the relative frequencies are shown in Fig. 6. It is clear that  $f_2/\langle f_2 \rangle$  becomes much more stable compared to the free-running operation, reaching a level of  $1 \times 10^{-10}$ . The Allan-deviation curves of  $f_1/\langle f_1 \rangle$  and  $F_r$  are almost identical, since  $f_2$  is stabilized. In the stabilization mode, the Allan deviation of  $f_1/\langle f_1 \rangle$  falls as a function of time more quickly, indicating the advantage of stabilizing leading magnetic field. The relative frequency  $f_1/\langle f_1 \rangle$  reaches approximately  $1 \times 10^{-9}$  at  $1 \times 10^4$  s. Note that the noise characteristics shown in Fig. 6 are somewhat different from those in Fig. 5, since

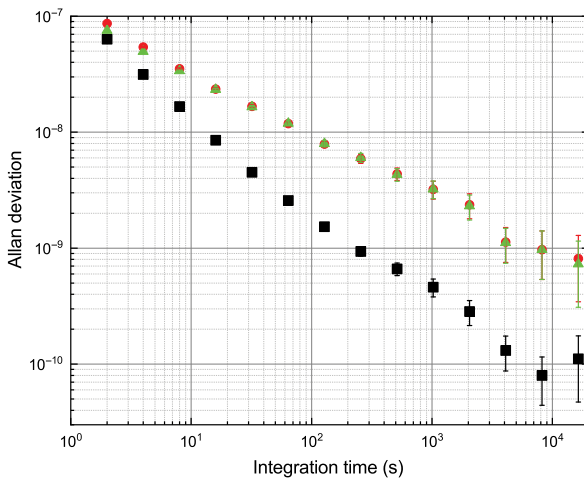


FIG. 6. The Allan deviation of the relative frequencies of the dual oscillators with the leading magnetic field stabilized by locking  $f_2$  to a reference frequency: black squares,  $f_2/\langle f_2 \rangle$ ; red circles,  $f_1/\langle f_1 \rangle$ ; green triangles,  $F_r$ . With  $f_2$  locked to a stable reference frequency, the roll-off of  $f_2/\langle f_1 \rangle$  and  $f_1/\langle f_1 \rangle$  gets quicker.

the feedback control changes the noise characteristics of the leading magnetic field.

The Allan deviation after  $4 \times 10^3$  s has relatively larger errors, due to both statistical error and low-frequency drift, as shown in Figs. 5 and 6. The Allan deviation of  $F_r$  in Fig. 5 is smaller than that of  $F_r$  based on the noise floor of  $f_c$  in Fig. 5 at the same integration time, possibly because of overestimating the noise of  $f_c$ , which contains not only intrinsic noise from atomic magnetometers but also external magnetic noise from the environment. The latter can be suppressed by feedback control of the leading magnetic field.

In order to find the inflection point of the Allan-deviation plot of  $F_r$ , we upgrade the program of the HF2LI to make it able to record the data for a longer time. Then we repeat the long-term stability experiment with the leading magnetic field stabilized several times. Two typical results for the Allan deviations of  $F_r$  are shown in Fig. 7. It is shown that the long-term stability of  $F_r$  varies. This phenomenon promotes us to measure the ambient temperature in the laboratory. The temperature measured by a Pt resistor located near the atomic cell is shown in Fig. 8. It shows that the actual temperature fluctuates remarkably in a time scale of weeks. The period with a relatively steady temperature only lasts for 2–3 days. The relation between  $F_r$  and the temperature is shown in Fig. 9, indicating that  $F_r$  varies with the temperature. Therefore, the stability of the OADOC is mainly limited by temperature fluctuations at present.

Compared with the single-species comagnetometer based on MSR, the OADOC acquires the two precession frequencies efficiently and simultaneously, resulting

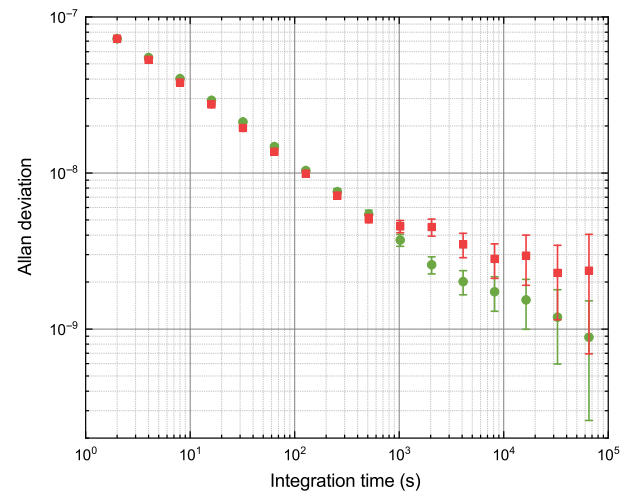


FIG. 7. The Allan deviations of  $F_r$ . The green circles and red squares denote two sets of experimental results.

in a remarkable improvement in sensitivity. The frequency ratio in the OADOC preserves the advantage of low drift. The  $F_r$  of OADOC with the free-running leading magnetic field reaches an instability of  $2 \times 10^{-9}$ , five times better than that of the MSR comagnetometer [18]. Moreover, the integration time of the former is less than 5% of that of the latter, although the frequency of the spin oscillator still has some systematic errors that need to be improved in the future [29]. With the leading magnetic field stabilized, the stability of  $F_r$  rolls off more quickly. The most important contribution to the low-frequency drift of the OADOC should be thermal fluctuation, which causes fluctuations of the magnetic field and laser parameters. The thermal drift could be reduced by a system-level thermal control. Compared with the optically orientated dual-maser comagnetometer, the OADOC is free from the light shift

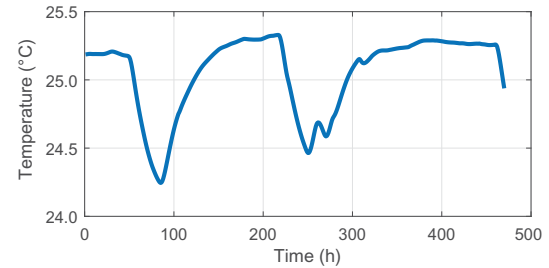


FIG. 8. The measured ambient temperature versus time for 20 days. Within this period, the temperature fluctuates severely in a long time scale, although the air conditioner is always set at  $24^\circ\text{C}$ . The temperature sensor of the air conditioner and the temperature-measuring device has an offset error but this does not matter, since we are only concerned with temperature fluctuations. The period in which the temperature fluctuates less than  $0.05^\circ\text{C}$  lasts for approximately 2–3 days.

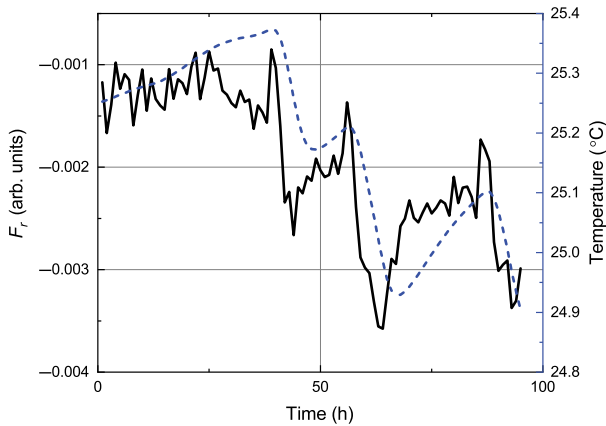


FIG. 9. The measured  $F_r$  and temperature versus time: black solid line,  $F_r$ ; blue dashed line, temperature. The data are smoothed using a first-order low-pass filter with a time constant of 10 000 s.

from pumping light and achieves better frequency stability, although the SNR is compromised. Compared with the single-species comagnetometer based on free-precession decay, the data-acquisition efficiency is improved [17].

The OADOC is more suitable for relative measurement, since there are several factors shifting the oscillation frequency from the corresponding magnetic resonance frequency for a spin oscillator. Rotation of the setup could shift the frequency ratio [15,30]. In the current leading magnetic field, the Earth's self-rotation will cause a maximum shift of  $2.8 \times 10^{-10}$ . Through correcting the rotation using a high-precision gyroscope, this effect can be decreased remarkably, so that it can be neglected at present. Through optimizing the cell temperature [23], the parameters in the HF2LI program and control loop [35], and the cell line width, the OADOC can be improved further, which would be studied in the future. On the whole, with  $F_r = 1 \times 10^{-9}$ , the OADOC has a potential to reach  $4 \times 10^{-19}$  eV for the measurement of the hypothetical spin-dependent gravitational energy of the proton [13,31].

#### IV. CONCLUSIONS

We realize a kind of comagnetometer utilizing a dual-frequency oscillator based on optically aligned  $^{87}\text{Rb}$  atoms. Due to the schemes of single species and optical alignment, the comagnetometer shows an excellent ability to suppress magnetic field fluctuations and a very small low-frequency drift. The frequency ratio of the comagnetometer with the free-running leading magnetic field reaches a stability of  $2 \times 10^{-9}$ , which is 5 times better than that of the MSR comagnetometer, since the oscillator operation improves the data-acquisition efficiency. Moreover, the stability of the frequency ratio reaches  $1 \times 10^{-9}$  after using one frequency oscillator for stabilizing the leading magnetic field and another frequency oscillator as a native observer of the local magnetic-field fluctuation. Through optimizing

the experimental parameters and employing a system-level thermal control, we can further improve the stability. As a whole, this kind of comagnetometer hopefully shows great potential in the measurement of spin-dependent exotic interactions.

#### ACKNOWLEDGMENTS

This research was supported by the National Natural Science Foundation of China (Grants No. 12174446, 61671458, 61571018, 61571003, and 91436210), and the Research Project of the National University of Defense Technology (Grant No. ZK17-02-04). Z.W. thanks Dr. Rui Zhang for helpful discussions.

- [1] A. L. Bloom, Principles of operation of the rubidium vapor magnetometer, *Appl. Opt.* **1**, 61 (1962).
- [2] D. Budker and M. Romalis, Optical magnetometry, *Nat. Phys.* **3**, 227 (2007).
- [3] T. Walker and M. Larsen, Spin-exchange-pumped NMR gyros, *Adv. Atom. Mol. Opt. Phys.* **65**, 373 (2016).
- [4] M. S. Safranova, D. Budker, D. DeMille, D. F. J. Kimball, A. Derevianko, and C. W. Clark, Search for new physics with atoms and molecules, *Rev. Mod. Phys.* **90**, 025008 (2018).
- [5] F. Allmendinger, W. Heil, S. Karpuk, W. Kilian, A. Scharth, U. Schmidt, A. Schnabel, Y. Sobolev, and K. Tullney, New Limit on Lorentz-Invariance- and CPT-Violating Neutron Spin Interactions Using a Free-Spin-Precession  $^3\text{He}$ - $^{129}\text{Xe}$  Comagnetometer, *Phys. Rev. Lett.* **112**, 110801 (2014).
- [6] M. A. Rosenberry and T. E. Chupp, Atomic Electric Dipole Moment Measurement Using Spin Exchange Pumped Masers of  $^{129}\text{Xe}$  and  $^3\text{He}$ , *Phys. Rev. Lett.* **86**, 22 (2001).
- [7] V. A. Kostelecký and C. D. Lane, Constraints on Lorentz violation from clock-comparison experiments, *Phys. Rev. D* **60**, 116010 (1999).
- [8] M. Bulatowicz, R. Griffith, M. Larsen, J. Mirjianian, C. B. Fu, E. Smith, W. M. Snow, H. Yan, and T. G. Walker, Laboratory Search for a Long-Range  $T$ -Odd,  $P$ -Odd Interaction from Axionlike Particles Using Dual-Species Nuclear Magnetic Resonance with Polarized  $^{129}\text{Xe}$  and  $^{131}\text{Xe}$  gas, *Phys. Rev. Lett.* **111**, 102001 (2013).
- [9] G. Vasilakis, J. M. Brown, T. W. Kornack, and M. V. Romalis, Limits on New Long Range Nuclear Spin-Dependent Forces Set with a  $\text{K}$ - $^3\text{He}$  Comagnetometer, *Phys. Rev. Lett.* **103**, 261801 (2009).
- [10] A. Yoshimi, K. Asahi, K. Sakai, M. Tsuda, K. Yogo, H. Ogawa, T. Suzuki, and M. Nagakura, Nuclear spin maser with an artificial feedback mechanism, *Phys. Lett. A* **304**, 13 (2002).
- [11] T. E. Chupp, R. J. Hoare, R. L. Walsworth, and B. Wu, Spin-Exchange-Pumped  $^3\text{He}$  and  $^{129}\text{Xe}$  Zeeman Masers, *Phys. Rev. Lett.* **72**, 2363 (1994).
- [12] A. Korver, D. Thrasher, M. Bulatowicz, and T. G. Walker, Synchronous Spin-Exchange Optical Pumping, *Phys. Rev. Lett.* **115**, 253001 (2015).

- [13] P. Bevington, R. Gartman, Y. V. Stadnik, and W. Chalupczak, Dual-frequency cesium spin maser, *Phys. Rev. A* **102**, 032804 (2020).
- [14] M. E. Limes, D. Sheng, and M. V. Romalis,  $^3\text{He}$ - $^{129}\text{Xe}$  Comagnetometry Using  $^{87}\text{Rb}$  Detection and Decoupling, *Phys. Rev. Lett.* **120**, 033401 (2018).
- [15] D. F. J. Kimball, I. Lacey, J. Valdez, J. Swiatlowski, C. Rios, R. Peregrina-Ramirez, C. Montcrieffe, J. Kremer, J. Dudley, and C. Sanchez, A dual-isotope rubidium comagnetometer to search for anomalous long-range spin-mass (spin-gravity) couplings of the proton, *Ann. Phys. (Berlin)* **525**, 514 (2013).
- [16] T. Wu, J. W. Blanchard, D. F. Jackson Kimball, M. Jiang, and D. Budker, Nuclear-Spin Comagnetometer Based on a Liquid of Identical Molecules, *Phys. Rev. Lett.* **121**, 023202 (2018).
- [17] Y. Yang, T. Wu, J. Chen, X. Peng, and H. Guo, All-optical single-species cesium atomic comagnetometer with optical free induction decay detection, *Appl. Phys. B* **127**, 40 (2021).
- [18] Z. Wang, X. Peng, R. Zhang, H. Luo, J. Li, Z. Xiong, S. Wang, and H. Guo, Single-Species Atomic Comagnetometer Based on  $^{87}\text{Rb}$  Atoms, *Phys. Rev. Lett.* **124**, 193002 (2020).
- [19] W. E. Bell and A. L. Bloom, Observation of Forbidden Resonances in Optically Driven Spin Systems, *Phys. Rev. Lett.* **6**, 623 (1961).
- [20] S. J. Ingleby, C. O'Dwyer, P. F. Griffin, A. S. Arnold, and E. Riis, Vector Magnetometry Exploiting Phase-Geometry Effects in a Double-Resonance Alignment Magnetometer, *Phys. Rev. Appl.* **10**, 034035 (2018).
- [21] P. L. Qi, X. X. Geng, G. Q. Yang, G. M. Huang, and G. X. Li, Theory of double-resonance alignment magnetometers based on atomic high-order multipole moments using effective master equations, *J. Opt. Soc. Am. B* **37**, 3303 (2020).
- [22] A. Weis, G. Bison, and A. S. Pazgalev, Theory of double resonance magnetometers based on atomic alignment, *Phys. Rev. A* **74**, 033401 (2006).
- [23] G. Di Domenico, H. Saudan, G. Bison, P. Knowles, and A. Weis, Sensitivity of double-resonance alignment magnetometers, *Phys. Rev. A* **76**, 023407 (2007).
- [24] G. Di Domenico, G. Bison, S. Groeger, P. Knowles, A. S. Pazgalev, M. Rebetez, H. Saudan, and A. Weis, Experimental study of laser-detected magnetic resonance based on atomic alignment, *Phys. Rev. A* **74**, 063415 (2006).
- [25] D. F. Jackson Kimball, J. Dudley, Y. Li, D. Patel, and J. Valdez, Constraints on long-range spin-gravity and monopole-dipole couplings of the proton, *Phys. Rev. D* **96**, 075004 (2017).
- [26] D. F. J. Kimball, Nuclear spin content and constraints on exotic spin-dependent couplings, *New J. Phys.* **17**, 073008 (2015).
- [27] Z. I. AG, HF2 User Manual (2022), [https://docs.zhinst.cn/pdf/ziHF2\\_UserManual.pdf](https://docs.zhinst.cn/pdf/ziHF2_UserManual.pdf).
- [28] B. Mathur, H. Tang, and W. Happer, Light shifts in the alkali atoms, *Phys. Rev.* **171**, 11 (1968).
- [29] Z. Wang, X. Peng, H. Luo, and H. Guo, Comparison of operation modes for spin-exchange optically-pumped spin oscillators, *J. Magn. Reson.* **278**, 134 (2017).
- [30] B. J. Venema, P. K. Majumder, S. K. Lamoreaux, B. R. Heckel, and E. N. Fortson, Search for a Coupling of the Earth's Gravitational Field to Nuclear Spins in Atomic Mercury, *Phys. Rev. Lett.* **68**, 135 (1992).
- [31] J. Mora, A. Cobos, D. Fuentes, and D. F. Jackson Kimball, Measurement of the ratio between *g*-factors of the ground states of  $^{87}\text{Rb}$  and  $^{85}\text{Rb}$ , *Ann. Phys. (Berlin)* **531**, 1800281 (2018).
- [32] D. W. Allan, Statistics of atomic frequency standards, *Proc. IEEE* **54**, 221 (1966).
- [33] W. J. Riley, *Handbook of Frequency Stability Analysis* (NIST Special Publication 1065, 2008) p. 15, <https://tf.nist.gov/general/pdf/2220.pdf>.
- [34] L. Shen, R. Zhang, T. Wu, X. Peng, S. Yu, J. Chen, and H. Guo, Suppression of current source noise with an atomic magnetometer, *Rev. Sci. Instrum.* **91**, 084701 (2020).
- [35] R. Zhang, Y. Ding, Y. Yang, Z. Zheng, J. Chen, X. Peng, T. Wu, and H. Guo, Active magnetic-field stabilization with atomic magnetometer, *Sensors* **20**, 4241 (2020).